Tellus (1995), 47A, 221–239
Printed in Belgium – all rights reserved

TELLUS
ISSN 0280–6495

Divergent wind analyses in the oceanic boundary layer

By SAROJA M. POLAVARAPU, *Data Assimilation and Satellite Meteorology Division, Atmospheric Environment Service, 4905 Dufferin Street, Downsview, Ontario, M3H 5T4, Canada*

(Manuscript received 18 March 1993; in final form 31 March 1994)

ABSTRACT

A method of analyzing the divergent part of the marine boundary layer flow is presented in the context of two-dimensional statistical interpolation. Instead of assuming geostrophic balance of observed minus background differences, a linearized Ekman balance is assumed. This results in correlation functions that are rotated with respect to the geostrophic correlation functions by a turning angle that is precisely the difference between the actual and geostrophic wind at mean sea level. The turning angle is also related to the degree to which divergent flow due to friction is analyzed; the larger the turning angle, the larger the extent of the analysis of divergent flow. Case studies comparing geostrophic and ageostrophic analyses show that changes to the pressure field occur when the turning angle is large and wind observations are sufficiently dense. Ageostrophic analyses are shown to contain divergent analysis increments and consequently, realistic wind analysis increments result.

1. Introduction

The aim of this work is to develop a method of analyzing the divergent component of marine boundary layer winds. Two primary factors motivate this research. (i) Since wind stress is the primary force driving ocean wave models, accurate representation of near surface winds over the ocean is needed for accurate forecasts of wave heights. Current operational objective analyses of marine winds are considered inadequate for these purposes by wave modelers (Cardone, 1992). Since surface winds are well correlated with surface geostrophic winds over the ocean only for periods longer than 4 days (Marsden, 1987), it is clear that a geostrophic wind analysis will not adequately analyze the high frequency part of the signal. The fact that analyses are typically derived from geostrophically balanced corrections to model trial fields may contribute to the inadequacy of marine wind analyses. (ii) With the recent launch of the ERS-1 satellite, scatterometer winds have become available to the data assimilation community. Since this data is available at high density (25 km), it is important to be able to analyze the mesoscale as well as the synoptic scale part of the flow in order to make "optimal" use of the data. Mesoscale flow is less quasi-non-divergent than is large scale flow so mesoscale analyses will require an adequate depiction of the divergent part of the flow. Early attempts to assimilate SEASAT-A scatterometer data were not encouraging (Baker et al., 1984; Duffy et al., 1984; Yu and MacPherson, 1984; Anderson et al., 1987; Ingleby and Bromley, 1991) but all of these studies required some form of balance between the rotational wind and the geopotential increments.

As a first step to considering the full three dimensional analysis problem, we focus upon the problem of assimilating marine wind data into two dimensional mean sea level analyses. Such analyses serve not only as input for wave models but also as a resource for meteorologists issuing a forecast. Currently, such analyses are performed at the Canadian Meteorological Centre (hereafter CMC) using a multivariate statistical interpolation scheme (see Mitchell et al., 1993; 1990 for details). In what follows, the statistical interpolation scheme shall provide the context within which we consider the problem of analyzing near surface marine winds. We relate this problem to the general problem of analyzing divergent flow first addressed by Daley (1985).

The paper is organized as follows: in Section 2 we derive a linear balance that includes a representation of friction. The impact of this balance on the form of the correlation functions is discussed in Section 3. Section 4 demonstrates that the Ekman analysis scheme presented in the previous section permits a locally varying analysis of the divergent wind. We then perform case studies comparing geostrophic and Ekman analyses (Section 5). The results are discussed in Section 6 and summarized in Section 7.

2. A representation of surface wind in terms of geostrophic wind

In this section, we present the physical context that motivates the analysis of divergence.

Consider the schematic representation of a boundary layer presented in Fig. 1. There are two layers within the boundary layer but the numerical weather prediction (hereafter NWP) model of CMC resolves explicitly only the upper layer. The surface layer, defined as a layer of constant fluxes (heat, momentum and moisture), exists below the model's lowest level. The top of the surface layer is assumed to correspond to the model's $\sigma = 1$ level, i.e., at the anemometer level. (In fact, the model's lowest level is well above the surface layer (see Delage, 1988a; 1988b) but for diagnostic purposes, winds and thermodynamic fields are output at 10 m and 2 m respectively. Thus we may assume that $\sigma = 1$ corresponds to the top of the surface layer.)

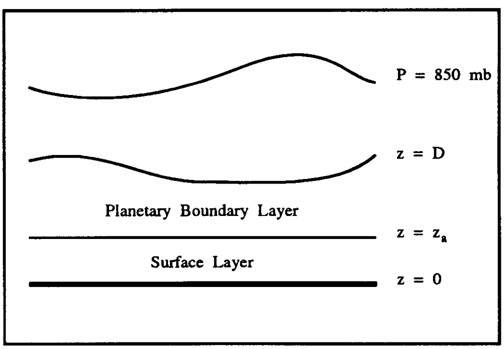

Fig. 1. Schematic diagram of assimilating model boundary layer. The lowest surface is the ocean. Above this is the anemometer level, then the top of the mixed layer and an 850 mb pressure surface.

Because geostrophic balance of the analysis increments is less reasonable in the PBL than in the free atmosphere, we shall assume an Ekman or antitriptic balance (e.g., Schafer and Doswell, 1980) through the planetary boundary layer (hereafter referring to only the upper layer and hereafter called PBL). That is, following Baker et al. (1987), we assume a three way balance between pressure gradient, Coriolis and frictional forces. In cartesian co-ordinates this may be written as

$$\frac{1}{\rho}\nabla_{\mathrm{H}} P + f\hat{\boldsymbol{k}} \times \boldsymbol{V} - \frac{1}{\rho}\frac{\partial \tau}{\partial z} = 0. \tag{2.1}$$

Here τ is the surface stress vector defined at the top of the surface layer, ρ is the atmospheric density, f the Coriolis parameter, P the scalar pressure and $\boldsymbol{V}$ the horizontal vector velocity, respectively. Clearly antitriptic balance can be expected to hold only under certain conditions. The omission of the inertial acceleration term assumes a steady state balance. Such a balance may be achieved only when the omitted processes operate on a time scale much longer than that required of the admitted forces. For example, we don't expect (2.1) to hold over the continents since land responds quickly to diurnal heating and such a steady balance could not routinely be established. Also, we do not expect (2.1) to hold in the tropics where inertial accelerations are of the same order as the terms in (2.1) (Haltiner, 1971). Thus antitriptic balance has no advantage over geostrophic balance in tropical regions. In using (2.1), we declare our interest solely in midlatitude oceanic regions.

In order to remove the nonlinearity in (2.1) and simplify the equation, we linearize the stress term about a first guess value, following Baker et al. (1987). Since $\tau = \tau_1 = 0$ at the top of the PBL and we define $\tau = \tau_0$ at the bottom of the PBL, we write

$$-\frac{1}{\rho}\frac{\partial \tau}{\partial z} \simeq -\frac{1}{\rho}\frac{\tau_1 - \tau_0}{D} = \frac{\tau_0}{\rho D}, \tag{2.2}$$

where D is the depth of the PBL. Since τ_0 is in the direction of the surface wind, (2.2) may be expressed as

$$-\frac{1}{\rho}\frac{\partial \tau}{\partial z} = \frac{|\tau_0|}{\rho D}\frac{\boldsymbol{V}_{\mathrm{a}}}{|\boldsymbol{V}_{\mathrm{a}}|} = \alpha \boldsymbol{V}_{\mathrm{a}} \tag{2.3}$$

where

$$\alpha = \frac{|\tau_0|}{\rho D\, |V_a|}. \tag{2.4}$$

Substituting (2.3) into (2.1) results in

$$\frac{1}{\rho}\nabla_H P + f\hat{k} \times V_a + \alpha V_a = 0. \tag{2.5}$$

On solving for u and v we obtain

$$u = -A\,\partial_x P - B\,\partial_y P, \tag{2.6}$$

$$v = B\,\partial_x P - A\,\partial_y P, \tag{2.7}$$

where

$$A = \frac{1}{\rho}\frac{\alpha}{\alpha^2 + f^2}, \qquad B = \frac{1}{\rho}\frac{f}{\alpha^2 + f^2}, \qquad \partial_j \phi = \partial\phi/\partial j. \tag{2.8}$$

Eqs. (2.6) and (2.7) are similar to those obtained by Baker et al. (1987) although their definitions of A and B are slightly different. Through the linearization of the stress term, we have expressed friction as a force proportional to velocity which acts in a direction opposite to the wind at the anemometer level. If we define

$$\partial_x P = \rho f v_g, \qquad \partial_y P = -\rho f u_g, \tag{2.9}$$

we may rewrite (2.6) and (2.7) as follows:

$$\begin{pmatrix} u \\ v \end{pmatrix} = \rho f \begin{pmatrix} B & -A \\ A & B \end{pmatrix} \begin{pmatrix} u_g \\ v_g \end{pmatrix}. \tag{2.10}$$

If we normalize matrix elements by the determinant of the matrix, substitute for A and B from (2.8), and use the following definition

$$\frac{f}{\sqrt{\alpha^2 + f^2}} = \cos\theta, \qquad \frac{\alpha}{\sqrt{\alpha^2 + f^2}} = \sin\theta, \tag{2.11}$$

we obtain

$$\begin{pmatrix} u \\ v \end{pmatrix} = \cos\theta \begin{pmatrix} \cos\theta & -\sin\theta \\ \sin\theta & \cos\theta \end{pmatrix} \begin{pmatrix} u_g \\ v_g \end{pmatrix} \tag{2.12}$$

$$= \frac{1}{2}\begin{pmatrix} u_g \\ v_g \end{pmatrix} + \frac{1}{2}\begin{pmatrix} \cos 2\theta & -\sin 2\theta \\ \sin 2\theta & \cos 2\theta \end{pmatrix} \begin{pmatrix} u_g \\ v_g \end{pmatrix}. \tag{2.13}$$

While (2.6)–(2.8) involve two new variables, A and B, (2.11) and (12.12) show that only one new variable θ, the turning angle, has been introduced.

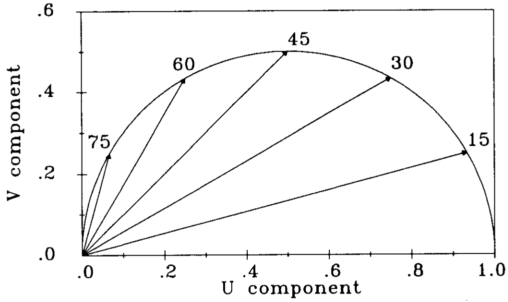

Fig. 2. The turning of the surface wind with friction. Plotted are anemometer level wind components for varying turning angles. Wind speeds are normalized. Angles are given in degrees.

As seen from (2.12), the horizontal wind vector is obtained from the geostrophic wind vector by a clockwise rotation of θ degrees and a reduction in speed by a factor $\cos\theta$. Equivalently one may view the wind vector at the top of the surface layer as half the sum of geostrophic wind plus a rotation of the geostrophic wind through an angle 2θ. Note that θ is given by

$$\theta = \tan^{-1}(A/B) = \tan^{-1}(\alpha/f). \tag{2.14}$$

For geostrophic flow, $\alpha = 0$ and hence $\theta = 0$. Fig. 2 illustrates the variation of the surface wind with turning angle. The coordinate system was chosen such that the x-axis lies along the direction of the geostrophic wind. Note that a semicircle with center $(0.5\,|V_g|, 0)$ defines the loci of all surface winds. This is predicted by (2.13) which shows the surface wind as the sum of $0.5\,|V_g|$ and a vector of the same magnitude rotated through an angle θ. Unlike the classic Ekman spiral diagram which illustrates the turning of the wind vector with height for the Ekman problem (e.g., Pedlosky, 1979, p. 181), what we illustrate is the wind vector at a given height (the top of the surface layer) for varying turning angles. We do not specify or calculate winds at other heights in the PBL because we are here concerned with the mean sea level (hereafter msl) analyses.

3. The influence of Ekman balance on analysis correlation functions

In Section 2, we obtained an expression relating winds at the top of the surface layer to horizontal pressure gradients, (2.6) and (2.7). While some assumptions regarding the structure of the PBL were made, it is always possible to relate the wind at the top of the surface layer to the wind above the PBL at a given location through a rotation and reduction. Thus the discussion in this section is in fact quite general. In this section we illustrate the influence of this more general linear balance on the forecast error correlation functions.

Now if both the truth and the model forecast variables are assumed to satisfy (2.6) and (2.7), then so must the forecast error:

$$u' = -A\,\partial_x P' - B\,\partial_y P', \tag{3.1}$$

$$v' = B\,\partial_x P' - A\,\partial_y P', \tag{3.2}$$

where the primes denote error (difference between truth and model forecast) quantities. Note that in forming (3.1) and (3.2) we have assumed that A and B are true fields although we will use background fields to calculate them. The impact of this assumption will be discussed in Section 6. We may now build our background error covariance model using (3.1), (3.2) to compute the covariances $(P_s^i u_s^j)$, $(u_s^i P_s^j)$, $(P_s^i v_s^j)$, $(v_s^i P_s^j)$, $(u_s^i v_s^j)$, $(v_s^i u_s^j)$, $(u_s^i u_s^j)$ and $(v_s^i v_s^j)$ in terms of the surface pressure autocovariance function. Angle brackets will denote correlations and hereafter, all variables are assumed to be error quantities so the primes have been dropped. The superscripts i and j correspond to the positions of analysis points i and j. The same correlation model used for geopotential heights on isobaric surfaces can be used for $(P_s^i P_s^j)$ except that the variances (which involve units) must be specific to mean sea level pressures. Thus, using the notation of Mitchell et al. (1990), we have

$$\operatorname{cov}(P_s^i P_s^j) = E_p^2 F(r), \tag{3.3}$$

$$\operatorname{cov}(P_s^i u_s^j) = [A^j \Pi + B^j \Xi]\,\mu E_p^2 F(r), \tag{3.4}$$

$$\operatorname{cov}(u_s^i P_s^j) = [-A^i \Pi - B^i \Xi]\,\mu E_p^2 F(r), \tag{3.5}$$

$$\operatorname{cov}(P_s^i v_s^j) = [-B^j \Pi + A^j \Xi]\,\mu E_p^2 F(r), \tag{3.6}$$

$$\operatorname{cov}(v_s^i P_s^j) = [B^i \Pi - A^i \Xi]\,\mu E_p^2 F(r), \tag{3.7}$$

$$\operatorname{cov}(u_s^i u_s^j) = [A^i A^j \Delta + B^i B^j \Gamma - A^i B^j \Theta - B^i A^j \Theta]\,E_p^2 F(r), \tag{3.8}$$

$$\operatorname{cov}(v_s^i v_s^j) = [B^i B^j \Delta + A^i A^j \Gamma + A^i B^j \Theta + B^i A^j \Theta]\,E_p^2 F(r), \tag{3.9}$$

$$\operatorname{cov}(u_s^i v_s^j) = [-A^i B^j \Delta + B^i A^j \Gamma - A^i A^j \Theta + B^i B^j \Theta]\,E_p^2 F(r), \tag{3.10}$$

$$\operatorname{cov}(v_s^i u_s^j) = [-B^i A^j \Delta + A^i B^j \Gamma - A^i A^j \Theta + B^i B^j \Theta]\,E_p^2 F(r). \tag{3.11}$$

Here, r is the horizontal distance between points i and j. The linear differential operators are defined in Appendix A. The use of superscripts for A and B indicates that boundary layer conditions (magnitude of the surface stress, PBL depth and anemometer level wind speed) and the Coriolis parameter vary horizontally. Note that the geostrophic coupling parameter μ (see Lorenc, 1981) is used in pressure-wind covariance functions (3.4) to (3.7). This is due to the fact (noted above) that antitriptic balance does not alleviate the problem of inapplicability in the tropics that was true of geostrophic balance. (3.3)–(3.11) are more general than the expressions used in Mitchell et al. (1990) in that the latter may be obtained simply by setting

$$\alpha = A^i = A^j = 0, \qquad B = B^i = B^j,$$

$$E_\psi = BE_p, \qquad E_z = E_p$$

in the above expressions, where E_ψ and E_z are forecast error standard deviations for stream function and height variables.

The correlation functions may be obtained from (3.3)–(3.11) on utilizing the following expressions for variance:

$$\operatorname{var}(P^i) = \operatorname{cov}(P^i P^i) = E_p^2, \tag{3.12}$$

$$\operatorname{var}(u^i) = \operatorname{cov}(u^i u^i) = [(A^i)^2 + (B^i)^2]\,E_p^2 L^{-2}, \tag{3.13}$$

$$\operatorname{var}(v^i) = \operatorname{var}(u^i), \tag{3.14}$$

where we have used the fact that

$$F(0) = 1, \quad F'(0) = 1, \quad F'(r) = -L^2 RF(r), \tag{3.15}$$

and

$$R = \frac{1}{r}\frac{\mathrm{d}}{\mathrm{d}r}, \qquad r^2 = (x_i - x_j)^2 + (y_i - y_j)^2. \tag{3.16}$$

Here L is a length scale of the correlation defined by

$$L^2 = -\left.\frac{F(r)}{F''(r)}\right|_{r=0},$$

and a prime denotes the nondimensional derivative defined in (3.15).

To understand how the correlations are influenced by the turning angle, it is useful to transform to polar coordinates as follows:

$$(x^i - x^j) = r\cos\phi,$$
$$(y^i - y^j) = r\sin\phi. \tag{3.17}$$

With the definitions (3.17) and (2.14), the correlations may be written as

$$\langle u^i P^j\rangle = \mu L^{-1}F'(r)[r\sin(\theta^i+\phi)],$$
$$\langle P^i u^j\rangle = -\mu L^{-1}F'(r)[r\sin(\theta^j+\phi)],$$
$$\langle v^i P^j\rangle = -\mu L^{-1}F'(r)[r\cos(\theta^i+\phi)],$$
$$\langle P^i v^j\rangle = \mu L^{-1}F'(r)[r\cos(\theta^j+\phi)],$$
$$\langle u^i u^j\rangle = \cos(\theta^i-\theta^j)\,F'(r) + RF'(r)[r^2\sin(\theta^i+\phi)\sin(\theta^j+\phi)],$$
$$\langle v^i v^j\rangle = \cos(\theta^i-\theta^j)\,F'(r) + RF'(r)[r^2\cos(\theta^i+\phi)\cos(\theta^j+\phi)],$$
$$\langle u^i v^j\rangle = -\sin(\theta^i-\theta^j)\,F'(r) - RF'(r)[r^2\sin(\theta^i+\phi)\cos(\theta^j+\phi)],$$
$$\langle v^i u^j\rangle = \sin(\theta^i-\theta^j)\,F'(r) - RF'(r)[r^2\cos(\theta^i+\phi)\sin(\theta^j+\phi)].$$

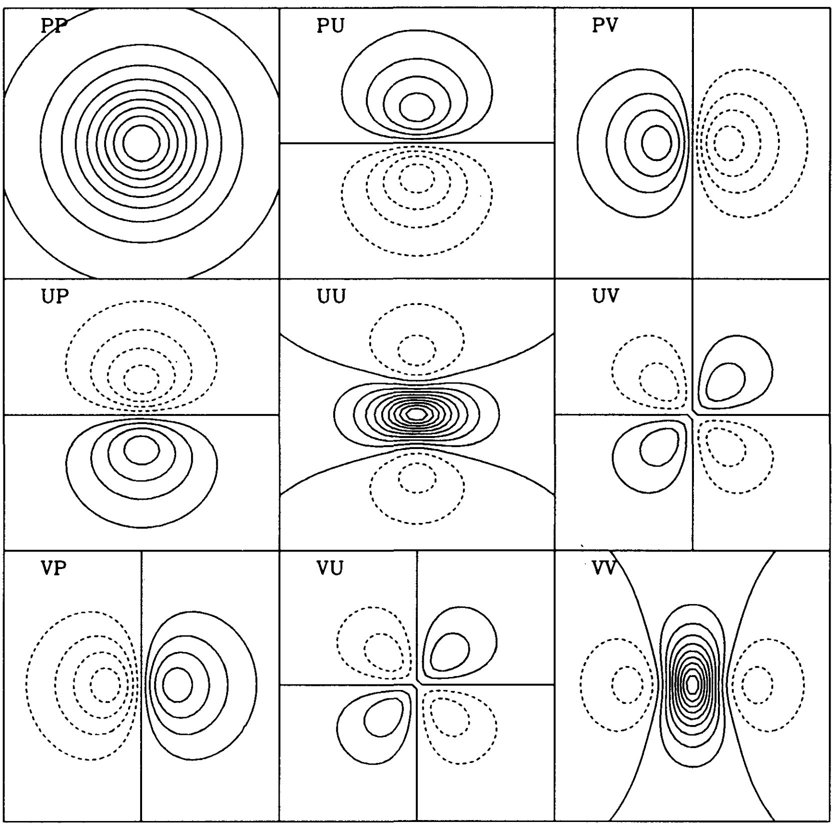

Fig. 3. The 9 correlation functions used for msl analyses for $\theta = 0$. Each frame is 2500 km × 2500 km. The contour interval is 0.1.

Let us first consider the special case in which α/f or θ is zero everywhere. Then the geostrophic correlations are recovered. The correlations become exactly those derived by Mitchell et al. (1990) (their equation (A3)) if we use the same $F(r)$ employed by them, namely, a third order autoregressive function defined in their (4). The correlations thus calculated are illustrated in Fig. 3. In computing Figs. 3 and 4, point i was chosen as the origin and point j was successively taken at each point in the frame in order to evaluate the correlation functions over the domain. Each frame is 2500 km in both zonal and meridional directions. The parameter c which appears in the definition of $F(r)$ of Mitchell et al. (1990) was set to 0.00537 km^{-1}, a value appropriate for the 30–60° latitude band.

Next, consider the special case in which α/f or θ is a constant. Then $\theta^i = \theta^j$ and the above correlations explicitly show that the correlation functions under Ekman balance are simply those obtained assuming geostrophic balance, but rotated by an angle θ. In other words, if $G_{\mathrm{up}}(r, \phi)$ is the geostrophic correlation for u^i and P^j, then $\langle u^i P^j \rangle = G_{\mathrm{up}}(r, \theta + \phi)$. Similar statements could be made for all the above correlations. Fig. 4 illustrates the 9 horizontal correlation functions for $\theta = 20°$.

In the case of a nonuniform θ, there is no simple convolution of the geostrophic correlations which leads to the general Ekman correlations. Most notable about the above expressions is the fact that $\langle u^i P^j \rangle \neq -\langle P^i u^j \rangle$, $\langle v^i P^j \rangle \neq -\langle P^i v^j \rangle$ and $\langle u^i v^j \rangle \neq \langle v^i u^j \rangle$. In fact this symmetry can only occur if $\theta^i = \theta^j$ over the analysis domain. This may occur, for example, for homogeneous flow conditions and constant f. Thus while the correlation function for $\langle P^i P^j \rangle$ is homogeneous and isotropic

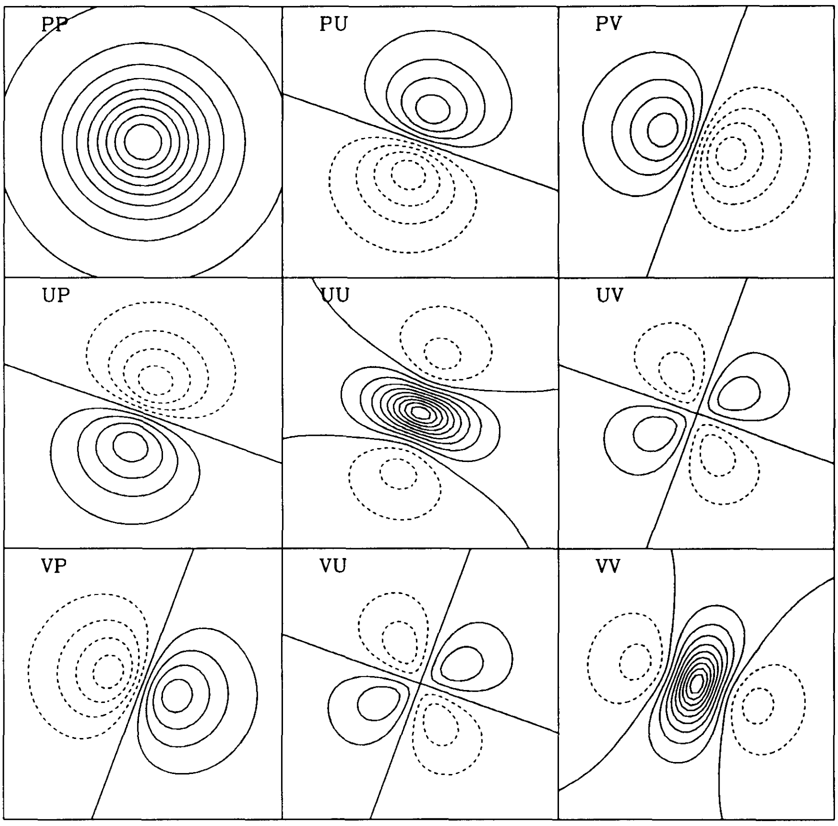

Fig. 4. As in Fig. 3 except for $\theta = 20°$.

in all cases, the remaining correlations are homogeneous for only the cases of geostrophy or a constant turning angle. In the general case, the other correlations depend on 4 parameters: r, ϕ, θ^i and θ^j and are neither homogeneous nor isotropic. Thus a pressure measurement at i and a wind measurement at j do not have the same correlation as a wind measurement at i and a pressure measurement at j. The reason why inhomogeneity of correlation functions arises when Ekman balanced forecast errors are assumed is that the wind can no longer be determined solely from a pressure field (as in the case of uniform flow or geostrophy). In addition to the pressure field, boundary layer conditions must be known as a function of space.

4. The analysis of divergence

Since the presence of a rigid boundary implies non-negligible vertical acceleration, the divergent component of the flow becomes important in the boundary layer. The use of Ekman balance at the lowest analysis level is a recognition of this fact. However, it is necessary to clarify the relationship between divergent flow analysis and Ekman analysis in order to fully comprehend the utility of the Ekman formulation of the covariance model. In this section, we show that the turning angle θ is simply related to a measure of the divergent flow analysis.

Following Daley (1985), we assume covariances of the form:

$$\mathrm{cov}(P_i P_j) = E_\mathrm{p}^2 K(r),$$

$$\mathrm{cov}(P_i \chi_j) = \mu E_\mathrm{P} E_\chi^j J(r),$$

$$\mathrm{cov}(\chi_i P_j) = \mu E_\mathrm{P} E_\chi^i J(r),$$

$$\mathrm{cov}(P_i \psi_j) = \mu E_\mathrm{P} E_\psi^j I(r),$$

$$\mathrm{cov}(\psi_i P_j) = \mu E_\mathrm{P} E_\psi^i I(r),$$

$$\mathrm{cov}(\psi_i \psi_j) = E_\psi^i E_\psi^j F(r),$$

$$\mathrm{cov}(\chi_i \chi_j) = E_\chi^i E_\chi^j G(r),$$

$$\mathrm{cov}(\psi_i \chi_j) = E_\psi^i E_\chi^j H(r),$$

$$\mathrm{cov}(\chi_i \psi_j) = E_\chi^i E_\psi^j H(r).$$

where the super or subscript $i(j)$ refers to quantities at point $i(j)$. The error variances of the divergent and rotational flow components are assumed to be a function of space. All covariances involving χ or ψ are nonhomogeneous and anisotropic but the correlations remain homogeneous and isotropic. Without approximation, we use Helmholtz's theorem to write u and v in terms of χ and ψ. Then employing the assumed forms for the covariances of pressure, stream function and velocity potential, we can derive the following expressions:

$$\mathrm{cov}(u_i u_j) = E_\psi^i E_\psi^j \Gamma F(r) + E_\chi^i E_\chi^j \Delta G(r) + (E_\psi^i E_\chi^j + E_\chi^i E_\psi^j)\,\theta H(r), \tag{4.1}$$

$$\mathrm{cov}(v_i v_j) = E_\psi^i E_\psi^j \Delta F(r) + E_\chi^i E_\chi^j \Gamma G(r) - (E_\psi^i E_\chi^j + E_\chi^i E_\psi^j)\,\theta H(r), \tag{4.2}$$

$$\mathrm{cov}(u_i v_j) = E_\psi^i E_\psi^j \theta F(r) - E_\chi^i E_\chi^j \theta G(r) + (-E_\psi^i E_\chi^j \Gamma + E_\chi^i E_\psi^j \Delta)\, H(r), \tag{4.3}$$

$$\mathrm{cov}(v_i u_j) = E_\psi^i E_\psi^j \theta F(r) - E_\chi^i E_\chi^j \theta G(r) + (E_\psi^i E_\chi^j \Delta - E_\chi^i E_\psi^j \Gamma)\, H(r), \tag{4.4}$$

$$\mathrm{cov}(P_i u_j) = -\mu E_\mathrm{p} E_\chi^j \Pi J(r) + \mu E_\mathrm{p} E_\psi^j \Xi I(r), \tag{4.5}$$

$$\mathrm{cov}(u_i P_j) = \mu E_\mathrm{p} E_\chi^i \Pi J(r) - \mu E_\mathrm{p} E_\psi^i \Xi I(r), \tag{4.6}$$

$$\mathrm{cov}(P_i v_j) = -\mu E_\mathrm{p} E_\chi^j \Xi J(r) - \mu E_\mathrm{p} E_\psi^j \Pi I(r), \tag{4.7}$$

$$\mathrm{cov}(v_i P_j) = \mu E_\mathrm{p} E_\chi^i \Xi J(r) + \mu E_\mathrm{p} E_\psi^i \Pi I(r). \tag{4.8}$$

Now, recall that Ekman balance is expressed by (2.6) and (2.7) and that the form of the covariances are correspondingly given by (3.3)–(3.11). Comparison of (3.3)–(3.11) with (4.1)–(4.8) yields

$$E_\chi^i = A^i E_\mathrm{p}, \qquad E_\psi^i = B^i E_\mathrm{p}, \tag{4.9}$$

$$G(r) = I(r) = K(r) = F(r), \quad H(r) = J(r) = -F(r). \tag{4.10}$$

(4.9) states that the error in stream function and velocity potential is related to the error in pressure at a given location. This accords with our previous assumption that A and B are true quantities, free from error. (4.9) also shows that the variances are inhomogeneous and anisotropic and the spatial inhomogeneity is entirely due to the boundary layer parameters. Thus we are incorporating Ekman balance by effectively weighting the error variances spatially, according to the boundary layer conditions at each point. As a result, the correlations remain homogeneous and isotropic.

In the special case where θ and f are simply constants, we can define parameters λ, λ^*, τ after Daley (1985):

$$G = F(r/\tau), \qquad H = \lambda F, \qquad I = \mu F,$$
$$J = \lambda^* F, \qquad K = F,$$

in order to compare the current problem with the more general one studied by Daley. Here $\tau = s_x/s$ where s_x and s are the length scales for the divergent and rotational components of the flow respectively, and μ, λ, λ^* are dimensionless constants. (4.10) implies that

$$\lambda = -1, \qquad \lambda^* = -1, \qquad \tau = 1.$$

Thus while Daley used 4 parameters, our special case requires only one: μ. The fact that $\tau = 1$ implies that $G = F$ and the streamfunction and velocity potential have identical autocorrelation functions. Thus corrections to the divergent and rotational components of the flow have the same spatial scale. $\lambda = -1$ implies that the $\psi - \chi$ cross-correlation function is the same as the $\psi - \psi$ and $\chi - \chi$ autocorrelations function and $\lambda^* = -1$ means that $\chi - P$ cross-correlations are handled similarly to $\psi - P$ cross-correlations with respect to the relaxation of the balance condition as the equator is approached. These simplifications arise because we consider only a special class of flows, namely, two-dimensional, steady flows with linearized stress, as defined by (2.6) and (2.7). These equations imply a direct (as opposed to a differential) relationship between vorticity and divergence, when θ and f are constant, namely,

$$\zeta = \cos^2\theta \frac{1}{\rho f}\nabla^2 P, \qquad \delta = -\cos\theta \sin\theta \frac{1}{\rho f}\nabla^2 P,$$

i.e.,

$$\delta = -(\tan\theta)\,\zeta. \tag{4.11}$$

The association of convergence or upward motion with geostrophic vorticity is a result of Ekman pumping which links the action of surface friction to dynamic processes in the free atmosphere. ψ and χ are also related by $\chi = -(\tan\theta)\,\psi$ so that errors in ψ and χ are not independent since θ is presumed error-free. Then, the auto-correlation functions should be the same ($\tau = 1$) and this implies that the $\psi - \chi$ cross-correlation function should equal the autocorrelation function ($\lambda = \lambda^* = -1$). Clearly for more general balances, other sources of divergence are possible. However (2.6), (2.7) consider only convergence due to frictional flow in the boundary layer.

In analogy with Daley's definition, we define a divergence parameter by

$$v^i = [E^i_{v_\chi}]^2\,[E^i_v]^{-2}, \tag{4.12}$$

where

$$(E^i_v)^2 = [E^i_{v_\chi}]^2 + [E^i_{v_\psi}]^2, \tag{4.13}$$

$$\begin{aligned} &[E^i_{v_\chi}]^2 = (E^i_\chi)^2/s_x^2,\\ &[E^i_{v_\psi}]^2 = (E^i_\psi)^2/s^2, \end{aligned} \tag{4.14}$$

where $s = s_x$ is assumed on the basis of the above discussion. v^i is a parameter representing the ratio of the prediction error variance of the divergent component of the flow to the prediction error variance of the total flow except that this parameter is determined locally, at each point. (2.14) may also be written more explicitly as

$$\theta^i = \tan^{-1}(A^i/B^i), \tag{4.15}$$

where θ^i is the local rotation of the correlation compared to the geostrophic correlations, at point i. Then substitution of (4.13)–(4.15) and (4.9) into (4.12) yields

$$\begin{aligned} &v^i = \sin^2(\theta^i),\\ &\frac{\alpha^i}{f^i} = \tan\theta^i = \sqrt{\frac{v^i}{1 - v^i}} \end{aligned} \tag{4.16}$$

v^i is the fraction of the total wind analysis represented by divergent flow. As the angle of rotation increases (assuming $0 \leqslant \theta \leqslant 90°$), the divergent component of the analyzed flow increases. For geostrophic flow, $\alpha = \theta = 0$ everywhere so $v = 0$ and the divergent component of the observation increment is not analyzed. At the other extreme, for $\theta = 90°$, the analysis increment is purely divergent. Intermediate values of θ produce wind analysis increments containing both rotational and divergent parts. Thus, the potential advantage of the Ekman balance formulation of the prediction error correlations is its ability to produce locally varying divergent wind analysis increments.

We now illustrate that only a small value of v is needed in order to obtain reasonable analyses of divergence. Fig. 5 graphically illustrates the relationships of (4.16). The function α/f, as seen in (2.5), is the ratio of the magnitude of friction to the Coriolis force. A value of zero indicates no friction, while a value of infinity indicates that rotation is unimportant for the flow under consideration. A value of 0.5 indicates friction forces of half the magnitude of the Coriolis forces. Fig. 5 shows that this corresponds to a turning angle of 27° and a value of $v = 0.2$. In fact, if Coriolis and friction are of the same order of magnitude, $\alpha/f = 1$ and $\theta = 45°$ and $v = 0.5$. Thus a reasonable upper limit to the turning angle is 45°. For more typical values of turning angle, say $\theta = 15°$, $\alpha/f = 0.27$ and $v = 0.07$. Thus even when the stress term is one quarter the magnitude of the Coriolis term, v remains quite small. As a result, large values of v and hence θ are not needed for an adequate analysis of divergence due to friction.

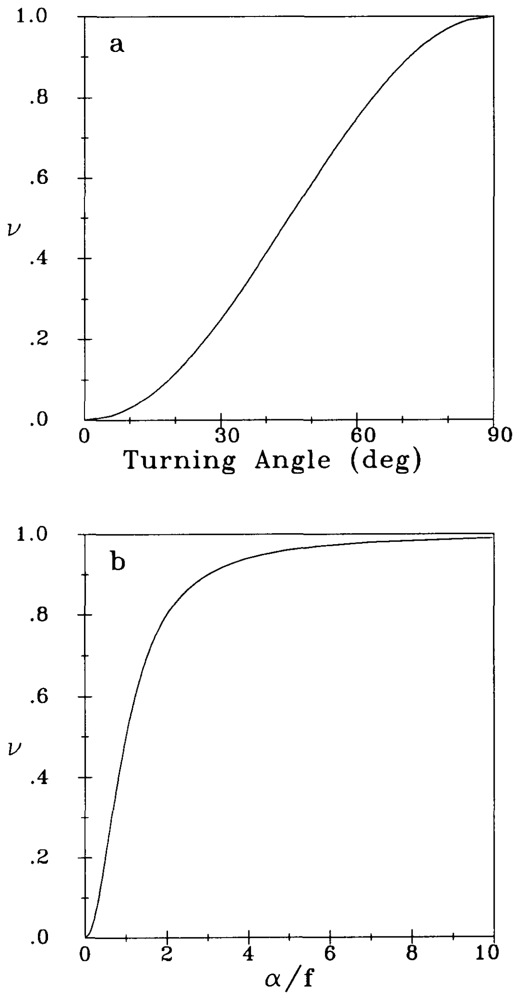

Fig. 5. The variation of divergence parameter, v, with (a) turning angle, θ, and (b) α/f.

5. Analyses performed with an operational data assimilation scheme

To perform the msl analyses, we employ the operational assimilation scheme of CMC (i.e., Mitchell et al., 1990). The following values for observation error variance were assumed:

$$\sigma^2_{\rm op} = 0.5\ \text{hPa}^2 \qquad \sigma^2_{\rm ou} = \sigma^2_{\rm ov} = 6.6\ \text{m}^2\,\text{s}^{-2}. \quad (5.1)$$

The background error variances are taken to be

$$\sigma^2_{\rm bp} = 1.5\ \text{hPa}^2 \quad \sigma^2_{\rm bu} = \sigma^2_{\rm bv} = \left[\frac{\cos\theta}{\rho f L}\right]^2 \sigma^2_{\rm bp}, \quad (5.2)$$

where θ is the turning angle. For a geostrophic covariance model, θ is 0 and $\sigma^2_{\rm bu} = 11.4\ \text{m}^2\,\text{s}^{-2}$. Since the data rejection criterion is a function of $\sigma^2_{\rm bu}$, by (5.2), it is a function of turning angle. Thus as the turning angle increases, the background error variances decrease and the rejection criterion becomes more strict. In addition, (5.2) suggests that background winds are perceived to be more accurate for divergent flow resulting from frictional forces. This is a consequence of the correlation model adopted (Section 4) and the assumption that the turning angle is error free. To avoid these problems, we modify the observation error variance to include the $\cos^2\theta$ term in order to retain a constant value for the ratio of observed to background wind error variances. As a result, we retain the same data rejection scheme and assign the same accuracies to wind observations for all analysis schemes whether geostrophic or ageostrophic. Since the actual value of the observation error variance is only used as the ratio to the forecast error variance, this seems a reasonable way to ensure the same quality control for all analyses regardless of the type of analysis.

Even in the absence of differences due to data rejection, differences may occur due to data selection. This procedure is used to reduce the problem of inverting a very large matrix (on the order of the number of observations) to one of inverting many smaller ones by analyzing each gridpoint separately and restricting the number of observations to the N most highly correlated with the analyzed point. Operationally $N=24$. In order to minimize such differences, N was increased to 60. To verify the independence of results to this parameter, identical analyses were compared for $N=60$ and $N=72$ and the differences were found to be negligible.

Prior to performing ageostrophic analyses, we must consider whether the turning angle field as calculated in Section 2 is meteorologically reasonable by examining the distribution of θ for a typical marine cyclone. Levy (1989) has shown that θ is a function of stability, thermal advection and baroclinicity. Thus, θ varies temporally as well as spatially, for a midlatitude storm. We expect large values where flow is highly ageostrophic at low levels, i.e., along the cold front. Also, since the ocean is comparatively warm, the boundary layer air in the warm sector of the maturing cyclone is more stable than that in the cold sector. Thus larger turning angles are expected in the warm sector. These hypotheses are supported by observations presented in Levy (1989).

To illustrate these ideas schematically, we first consider how vorticity and divergence impact the pressure analysis. Differentiation of (2.6) and (2.7) and substitution of (2.14) into the result yields the following expressions for vorticity ζ and divergence δ:

$$\zeta = \cos^2\theta \frac{1}{\rho f}\nabla^2 P + \cos 2\theta\, V_g \cdot \nabla\theta - \sin 2\theta \frac{1}{\rho f}\nabla P \cdot \nabla\theta \tag{5.3}$$

$$-\delta = \cos\theta \sin\theta \frac{1}{\rho f}\nabla^2 P + \sin 2\theta\, V_g \cdot \nabla\theta + \cos 2\theta \frac{1}{\rho f}\nabla P \cdot \nabla\theta \tag{5.4}$$

In deriving (5.3) and (5.4), the Coriolis parameter was assumed to be constant. This is because in the operational analysis scheme, background wind error variances vary slowly with latitude, which from (5.2) implies that the same is true of the correlation width, L, and the Coriolis parameter. If θ is a constant, (5.3) and (5.4) show that $\delta = -\zeta \tan\theta$, i.e., that divergence is a multiple of the vorticity. Thus convergence (divergence) is associated with cyclonic (anticyclonic) vorticity and as θ increases for a given wind observation increment, the divergence increases. If θ is not constant, it is easier to determine its effect on pressure analyses indirectly by examining its influence on vorticity and divergence as in (5.3) and (5.4). Fig. 6 is a schematic illustration of the θ field for a midlatitude cyclone. The solid black lines represent background field isobars at msl and the shaded region denotes the area of large turning angle which encompasses warm sector and frontal regions. The regions where the terms involving θ gradients in (5.3)–(5.4) are nonzero are also indicated. The term $B = V_g \cdot \nabla\theta$ is nonzero when θ gradients have a component parallel to the geostrophic wind direction. On the other hand, the term $C = (1/\rho f)\nabla P \cdot \nabla\theta$ is largest where θ gradients and pressure gradients are similarly oriented. C is positive when the gradient vectors point in the same direction and negative when they point in opposite directions. For nonconstant θ,

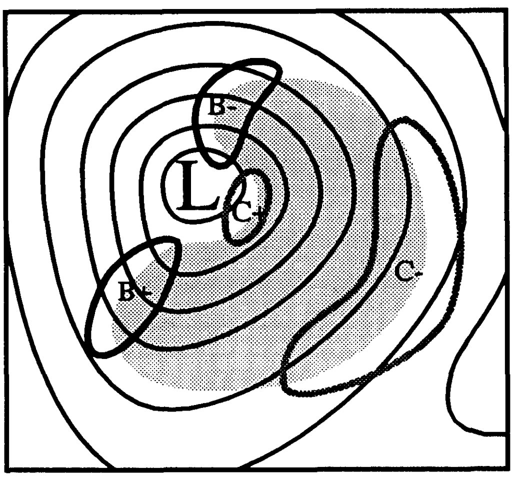

Fig. 6. Schematic diagram illustrating the influence of nonconstant turning angle on msl pressure analyses. The contours depict an msl pressure background field. The region of large turning angles is shaded. The heavy black lines identify regions where the term $B = V_g \cdot \nabla\theta$ is nonzero and the heavy grey lines mark regions where $C = (\rho f)^{-1}\nabla P \cdot \nabla\theta$ is nonzero.

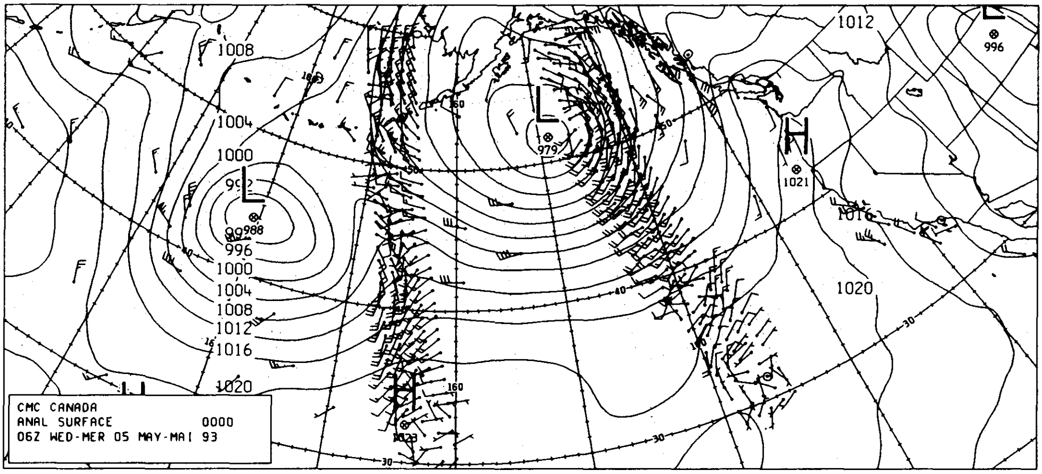

Fig. 7. The operational analysis and data distribution for 0600 UTC 5 May 1993.

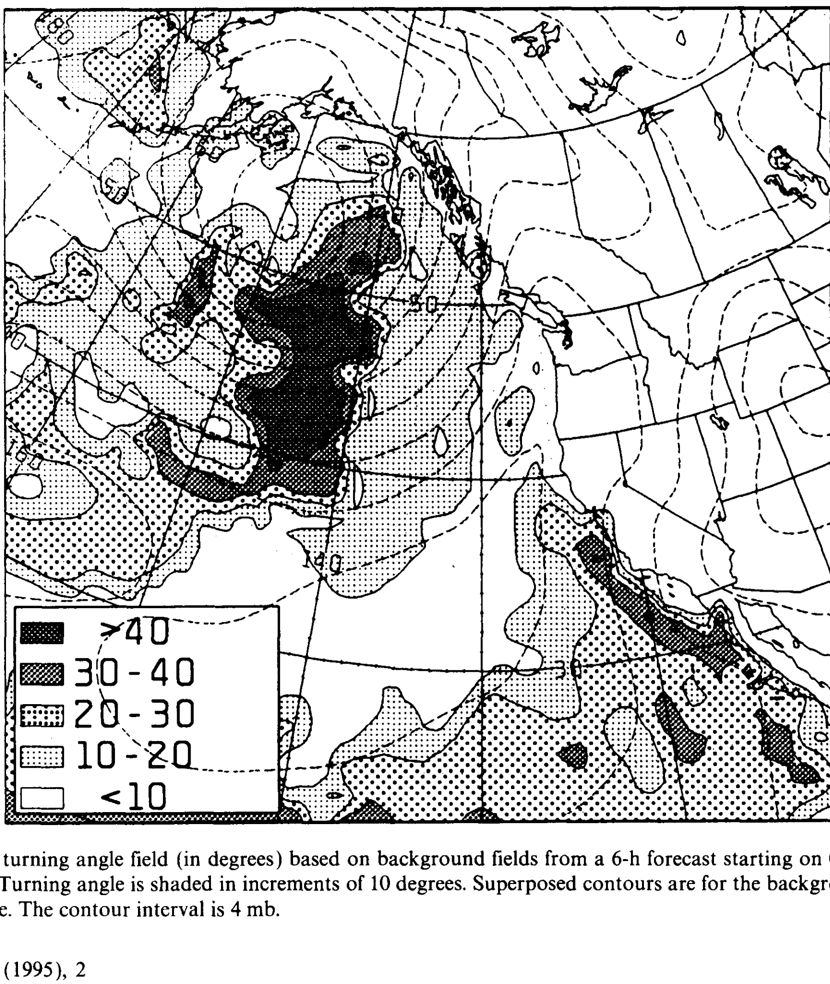

Fig. 8. The turning angle field (in degrees) based on background fields from a 6-h forecast starting on 0000 UTC 5 May 1993. Turning angle is shaded in increments of 10 degrees. Superposed contours are for the background field of msl pressure. The contour interval is 4 mb.

the first terms dominate the right sides of (5.3) and (5.4) since the θ gradient is at most $\pi/4$ per grid length (or 4×10^{-6} m^{-1} for 200 km grid spacing). Thus the last two terms are large only where the geostrophic wind speed or pressure gradient is very large, i.e., near cyclone centres. Where B is positive, the third term contributes toward vorticity and convergence. Where C is negative the 4th terms in (5.3) and (5.4) are likely to be small. Where C is positive, these terms contribute toward convergence and decreased vorticity. Since the positive regions are roughly in the vicinity of the cold front, enhanced divergent flow in these regions accords with our conceptual model of midlatitude cyclones (e.g., Shapiro and Keyser, 1990).

5.1. *Pressure analyses*

In order for divergent wind observations to impact pressure analyses, the flow should possess a significant ageostrophic component and it should be adequately sampled. Thus we sought to analyze cases involving deep cyclones depicted by numerous wind observations. It was difficult to find such cases despite the availability of scatterometer data since typically only one data swath (in a 6-h data window) would be found to cover an extensive section of a marine cyclone. However, the case we have chosen does have two swaths of scatterometer data available. The operational analysis for this case on 0600 UTC 5 May 1993 is shown in Fig. 7. A low center of 979 hPa was

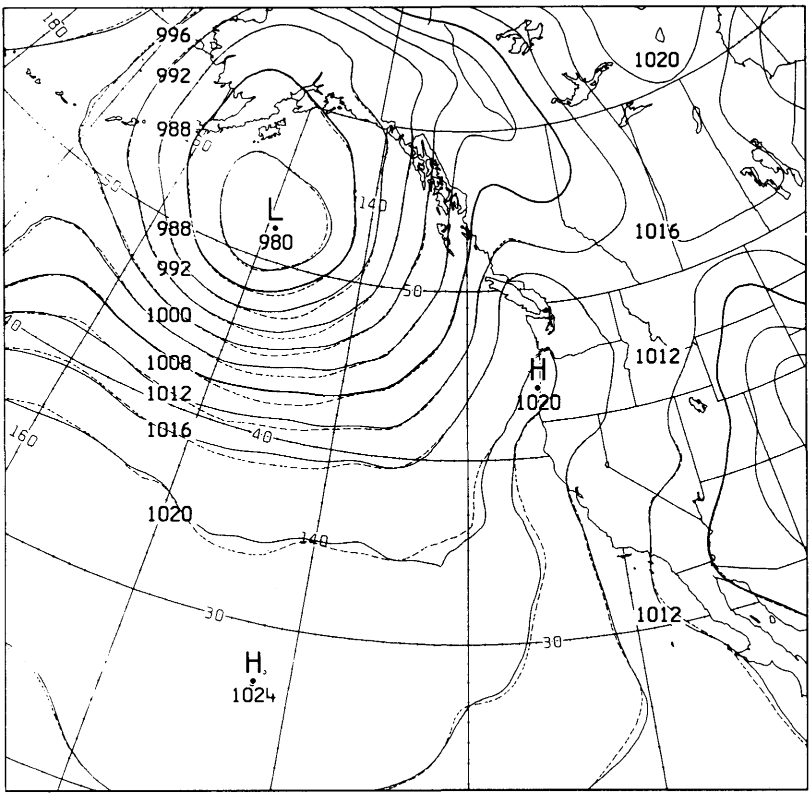

Fig. 9. Comparison of msl pressure analyses for geostrophic (solid lines) and ageostrophic (dotted lines) cases for 0600 UTC 5 May 1993. The ageostrophic analysis used the turning angle field of Fig. 8. Both analyses used scatterometer data. Contours are given every 4 mb.

analyzed south of Alaska. This depression was moving eastward and filling prior to the analysis time. A minimum pressure of 968 hPa was analyzed on 0000 UTC 3 May 1993. One swath passed close to the low center at approximately 0730 UTC. The second swath passed over a ridge of high pressure to the west of the low at approximately 0930 UTC. Globally, 3515 land stations, 440 ships, 112 buoys, 300 drifting buoys and 400 scatterometer winds were used. Note that the scatterometer data was thinned to a resolution of 100 km to avoid overwhelming data selection procedures (Hoffman, 1993). Additionally, scatterometer winds were assimilated identically to ship winds; the same observation error variance was used and no horizontal correlations were assumed.

The turning angle for this case is indicated in Fig. 8. Note that large values appear in a trough south of the low center in a region well sampled by scatterometer data. Corresponding to the interpretation of Fig. 6, the region of large turning angle suggests the position of an occluded front. The geostrophic and ageostrophic analyses are indicated in Fig. 9. With scatterometer data, the low center is analyzed as 980 hPa. Differences due to the ageostrophic analysis are slight but appear precisely where θ and its gradient is large, south of the low center. An ageostrophic analysis with $\theta = 20°$ everywhere (not shown) resulted in little difference over the geostrophic analysis although using $\theta = 45°$ everywhere (not shown) did capture the slightly deeper trough of the ageostrophic analysis (with θ as depicted in Fig. 8). However, the analysis with $\theta = 45°$ also differed from the geostrophic analysis at the position of the second data swath. The ageostrophic analysis of Fig. 9 did not differ from the geostrophic analysis there since

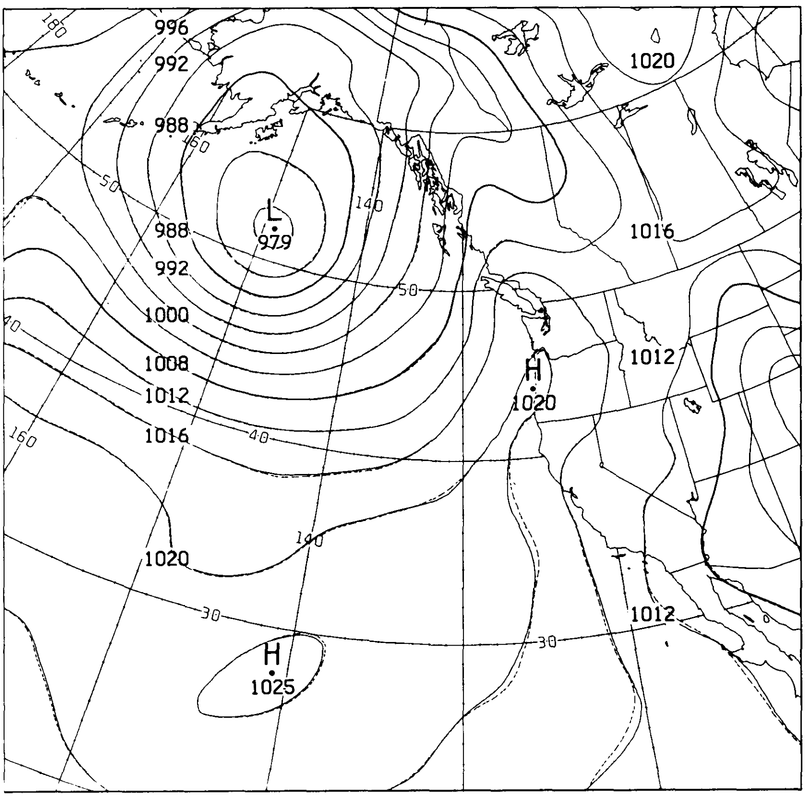

Fig. 10. As in Fig. 9 except analyses did not use scatterometer data.

θ is small in that region. Thus the potential advantage of using a spatially varying turning angle is that when observations depict geostrophic flow, the analysis will be geostrophic where θ is small. In practice, large values typically appear in the vicinity of cyclones so that outside of these regions, the geostrophic assumption is used.

Since no independent analyses were available to determine which analysis is "better", we can only conclude that the ageostrophic analysis will differ from the geostrophic analysis where there are large gradients in pressure and the turning angle is large and/or has large gradients, as expected from (5.3) and (5.4). However, it is also necessary to have fairly dense wind observations. This is seen in Fig. 10 by comparing geostrophic and ageostrophic analyses in the absence of scatterometer data. Without plenty of wind observations, the pressure analysis is largely determined from pressure data (which is treated univariately) and is therefore insensitive to the turning angle. With data selection, this is also true for each analysis point. Thus

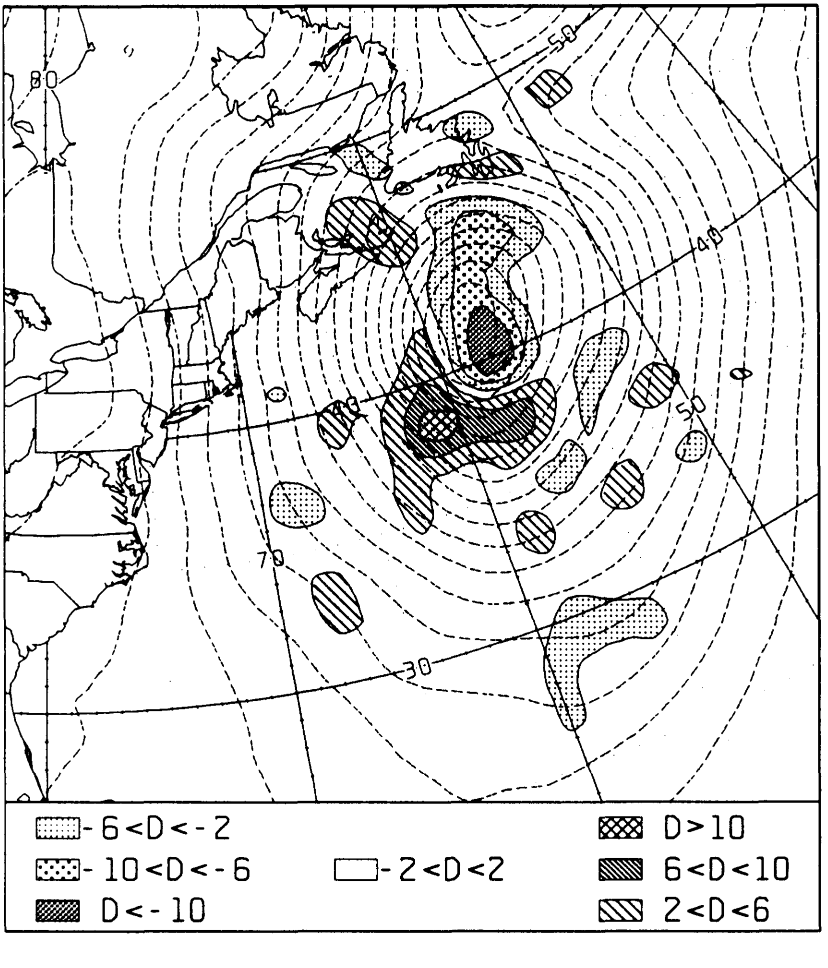

Fig. 11. Divergent part of wind analysis increments for 0000 UTC 5 January 1989 for the Ekman analysis employing a horizontally varying turning angle field. Values are scaled by 10^5 and areas of divergence greater than $2 \times 10^{-5}\ s^{-1}$ in absolute value are shaded. The corresponding msl pressure analysis is also shown (dashed lines) for a contour interval of 4 mb.

the number of winds in the search readius around a given analysis point should compare to the number of pressure observations for a change in turning angle to impact the analysed pressure.

5.2. *Wind analyses*

We have chosen to illustrate wind analyses with a case study of an ERICA (Experiment on Rapidly Intensifying Cyclones over the Atlantic; Hadlock and Kreitzberg, 1988; 1991) storm at 0000 UTC 5 January 1989. This storm's central pressure deepened by 60 hPa in 24 h, reaching a maximum depth of 936 hPa near the analysis time (Neiman and Shapiro, 1993). For this case, 2318 land, 676 ships and 135 buoy reports were used. The strength of this storm clearly warrants an ageostrophic analysis yet the ageostrophic pressure analysis differed little from the geostrophic pressure analysis since only 20% of the observations were winds and also because of the spacing of wind observations, as discussed above. However, the strength of the observed ageostrophic flow clearly impacts wind analyses. Examination of vorticity increments (not shown) reveals a correlation of cyclonic vorticity with negative pressure increments and anticyclonic vorticity with positive increments. The divergence of wind analysis increments shown in Fig. 11 has a similar pattern with convergence (divergence) associated with negative (positive) pressure increments just downstream (upstream) of the low centre. Maximum values are in excess of $10^{-4}\,s^{-1}$ while for the geostrophic analysis, the divergence increments are negligible, as expected. For a

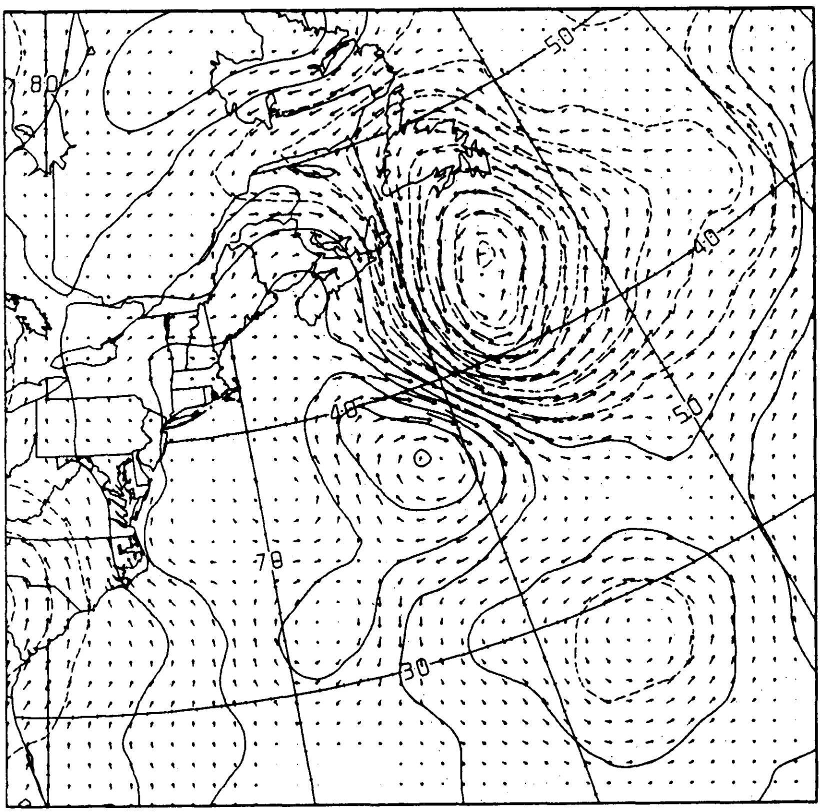

Fig. 12. Analysis increments for a geostrophic analysis for 0000 UTC 5 January 1989. Pressure analysis increments are contoured every 1 mb with negative contour levels dashed. Wind analysis increments are shown as vectors.

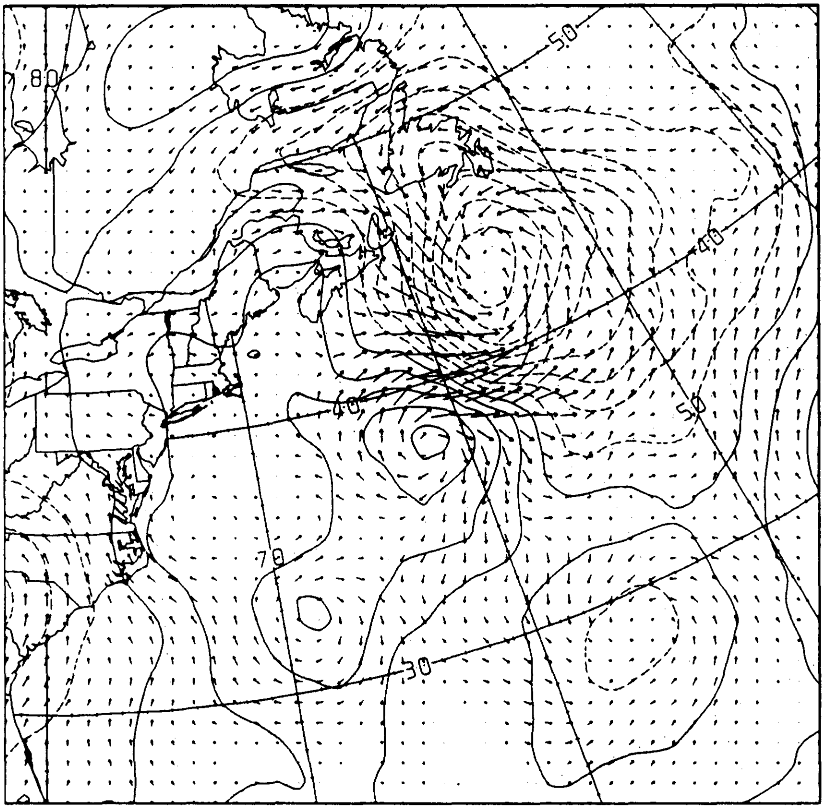

Fig. 13. As in Fig. 12 except for an ageostrophic analysis with spatially varying turning angle.

constant turning angle of 20°, a similar pattern of divergence (to Fig. 11) was found but with roughly half the magnitude.

The wind and pressure analysis increments for the geostrophic analysis are shown in Fig. 12. The corresponding analysis increments for the ageostrophic analysis employing a spatially varying turning angle are seen in Fig. 13. In Fig. 13, strong convergence is associated with negative pressure increments in the region (50–60° W, 40–50° N) downstream of the storm centre, in sharp contrast to Fig. 12. Similarly, the divergent flow centred at (61° W, 38° N) in Fig. 13 is not seen in Fig. 12 nor is the convergence centred at (56° W, 29° N) due to a pressure trough (Fig. 11). Clearly Fig. 13 depicts more reasonable analysis increments than Fig. 12, given the strength of the storm.

While ERICA IOP4 was an extremely deep depression, even for the more modest Pacific storm of Figs. 7–10, the divergence for the ageostrophic analysis using θ as in Fig. 7 was often 2–3 times the magnitude of that resulting from a similar analysis but with $\theta = 20°$ everywhere.

6. Discussion

It is common that the weakness of any scheme lies primarily in its assumptions. We now examine each assumption in turn for its validity. To start, as shown in Section 3, the use of a linearized Ekman balance has the effect of rotating the correlation functions. In general, it is a dangerous practice to arbitrarily alter correlation functions which are empirically derived estimates of the background error structure. However, in this case, the angle of rotation of the correlations is derived from background fields and the imposed Ekman balance is arguably more compatible with the background fields than is geostrophic balance. In other words, since a turning angle field exists independent of the analysis scheme, we might view the geostrophic analysis as more inconsistent since it arbitrarily sets all turning angles to zero.

In (3.3)–(3.11), the coefficients A and B (and hence the turning angle) are assumed to be "true" although they are estimated from background variables. As a result, if a cyclone is displaced in background fields from its "true" position, the turning angle field will also be displaced and the resulting analysis will be in error. Of course this problem is not specific to the Ekman analysis; it also affects the geostrophic analysis. One method of dealing with poorly placed cyclones in the background field is to define an iterative sequence. The analysis may be used to compute the difference between the geostrophic and analyzed wind fields, i.e., a new turning angle field, which can be compared with that based on the background fields. The original turning angle field may be relaxed toward the new one and the analysis recomputed. The turning angle field may thus be updated in an iterative fashion. Such a sequence presumes that the correct cyclone position is well defined by the data and is hence contained in the "analyzed" turning angle field.

An important assumption is the linear decrease of stress in the marine boundary layer which permits the linearization of the stress term and the formulation of a linear Ekman balance. Recall that such an assumption is not made by the assimilating boundary layer model and hence there is an inconsistency between the analysis and the model boundary layer. The justification for approximating the vertical stress profile is that it is better than discounting the boundary layer altogether.

The linear balance considered in (2.5) may be viewed as an extension of the "linear balance equation" which incorporates friction. Explicitly, if we write (2.5) in terms of geopotential and take $\nabla \cdot (2.5)$ we obtain

$$\nabla^2\phi - \nabla \cdot f\nabla\psi + \nabla \cdot f\boldsymbol{k} \times \nabla\chi + \nabla \cdot \alpha\,\nabla\chi + \nabla \cdot \alpha\boldsymbol{k} \times \nabla\psi = 0. \tag{7.1}$$

where

$$\boldsymbol{V} = \boldsymbol{V}_\psi + \boldsymbol{V}_\chi = \boldsymbol{k} \times \nabla\psi + \nabla\chi.$$

The linear balance equation results on assuming no friction ($\alpha = 0$) and divergent motions much smaller that rotational motions:

$$\nabla^2\phi - \nabla \cdot f\nabla\psi = 0. \tag{7.2}$$

A different simplification of (7.1) which was discussed in Section 4 arose on assuming α, f and θ to be constants. In that case, vorticity and divergence are related by (4.11) and because α/f is constant, ψ and χ are related by

$$\alpha/f\psi + \chi = 0, \tag{7.3}$$

and (7.1) simplifies to

$$\nabla^2\phi - f\sec^2\theta\,\nabla^2\psi = 0. \tag{7.4}$$

However, other simplifications are possible and result in intermediate balances. In particular, if α and f vary with latitude but θ is constant (7.1) becomes

$$\nabla^2\phi - \nabla \cdot f\nabla\psi + \nabla \cdot \alpha\,\nabla\chi = 0. \tag{7.5}$$

This may be viewed as a generalization of (7.4) which includes the β-effect or as an extension of the linear balance equation, (7.2), which incorporates friction.

7. Summary

In this paper, we have presented a method of analyzing wind data from the marine boundary layer. Instead of assuming geostrophic balance between observed minus background residuals, a linearized Ekman balance is assumed. That is, a three-way balance between pressure gradient, Coriolis and frictional forces is enforced. The inclusion of this frictional term has the effect of rotating the correlation functions. In addition, it permits the analysis of the divergent part of the wind increments. We have shown that the extent to which the divergent part of the wind increments is analyzed is measured by the turning angle between the geostrophic and background wind fields at the analysis level (msl). As this turning angle increases from 0 to $\pi/2$, the magnitude of the divergent part of the analyzed flow increases. A value of 0 produces a geostrophic analysis while a value of $\pi/2$ produces a purely divergent analysis. By estimating the turning angle at each point using background boundary layer variables, a locally varying analysis of divergence is produced. Case studies show an impact of wind observations on pressure analyses when they are sufficiently numerous and densely spaced. The impact on wind analyses is to produce divergent analysis increments where the turning angle is large, primarily in the vicinity of cyclones. The resulting analyzed flow is, qualitatively, more realistic than that produced from a geostrophic analysis.

8. Acknowledgements

I thank Bruce Brasnett, Cécilien Charette and Clément Chouinard whom I often consulted while becoming familiar with the Fortran programs used in the operational analysis scheme of CMC. John Filipkowski wrote the scripts to handle observational data formats. Roger Daley, Pierre Gauthier, Ross Hoffman, Herschel Mitchell, Dave Steenbergen and two anonymous reviewers provided helpful comments on earlier versions of this manuscript. I am especially grateful to Roger Daley for his encouragement of this work from its earliest stages. Special thanks to the European Space Agency for providing the ERS-1 scatterometer data.

9. Appendix A

Linear differential operators used in text

$$\Gamma = -[R + (y_i - y_j)^2 R^2], \tag{A1}$$

$$\Delta = -[R + (x_i - x_j)^2 R^2], \tag{A2}$$

$$\Theta = (y_i - y_j)(x_i - x_j) R^2, \tag{A3}$$

$$\Xi = (y_i - y_j) R, \tag{A4}$$

$$\Pi = (x_i - x_j) R, \tag{A5}$$

where

$$R = \frac{1}{r}\frac{\mathrm{d}}{\mathrm{d}r}, \tag{A6}$$

$$r^2 = (x_i - x_j)^2 + (y_i - y_j)^2. \tag{A7}$$

REFERENCES

Anderson, D. L., Hollingsworth, A., Uppala, S. and Woiceshyn, P. 1987. *A study of the feasibility of using sea and wind information from the ERS-1 satellite.* ECMWF Contract Report No. 6297/86/HGE-I(SC).

Baker, W. E., Atlas, R., Kalnay, E., Halem, M., Woiceshyn, P. M., Peteherych, S. and Edelmann, D. 1984. Large-scale analysis and forecast experiments with wind data from the Seasat A scatterometer. *J. Geophys. Res.* **89**, 4927–4936.

Baker, W. E., Bloom, S. C., Woollen, J. S., Nestler, M. S., Brin, E., Schlatter, T. W. and Branstator, G. W. 1987. Experiments with a three-dimensional statistical objective analysis scheme using FGGE data. *Mon. Wea. Rev.* **115**, 272–296.

Cardone, V. J. 1992. On the structure of the marine surface wind field in extratropical storms. Preprints of *3rd International Workshop on Wave hindcasting and forecasting*, 19–22 May 1992, Montréal, Québec. Environment Canada, Atmospheric Environment Service, 4905 Dufferin Street, Downsview, Ontario, Canada, M3H 5T4. 54–66.

Daley, R. 1985. The analysis of synoptic scale divergence by a statistical interpolation procedure. *Mon. Wea. Rev.* **113**, 1066–1079.

Daley, R. 1991. *Atmospheric data analysis.* Cambridge Univ. Press. 457 pp.

Delage, Y. 1988a. A parameterization of the stable atmospheric boundary layer. *Boundary-Layer Meteor.* **43**, 365–381.

Delage, Y. 1988b. The position of the lowest levels in the boundary layer of atmospheric circulation models. *Atm.-Ocean* **26**, 329–340.

Duffy, D., Atlas, R., Rosmond, T., Barker, E. and Rosenberg, R. 1984. The impact of Seasat scatterometer winds on the Navy's operational model. *J. Geophys. Res.* **89**, 7238–7244.

Hadlock, R. and Kreitzberg, C. W. 1991. Overview of the ERICA field phase. Proceedings of *First International Symposium on Winter Storms.* 14–18 January 1991, New Orleans, Amer. Met. Soc., Boston, Mass., 103–107.

Hadlock, R. and Kreitzberg, C. W. 1988. The experiment on rapidly intensifying cyclones over the Atlantic (ERICA) field study: objectives and plans. *Bull. Amer. Meteor. Soc.* **69**, 1309–1320.

Haltiner, G. J. 1971. *Numerical weather prediction.* John Wiley and Sons, 317 pp.

Hoffman, R. N. 1993. A preliminary study of the impact of the ERS 1 C Band scatterometer wind data on the European Centre for Medium-Range Weather Forecasts global data assimilation system. *J. Geophys. Res.* **98**, 233–244.

Ingleby, N. B. and Bromley, R. A. 1991. A diagnostic study of the impact of Seasat scatterometer winds on numerical weather prediction. *Mon. Wea. Rev.* **119**, 84–103.

Levy, X. 1989. Surface dynamics of observed maritime fronts. *J. Atmos. Sci.* **46**, 1219–1232.

Lorenc, A. 1981. A global three-dimensional multivariate statistical interpolation scheme. *Mon. Wea. Rev.* **109**, 701–721.

Marsden, R. F. 1987. Comparison between geostrophic and directly measured surface winds over the Northeast Pacific Ocean. *Atm.-Ocean* **25**, 387–401.

Mitchell, H. L., Charette, C., Lambert, S. J., Hallé, J. and Chouinard, C. 1993. The Canadian global data assimilation system: description and evaluation. *Mon. Wea. Rev.* **121**, 1467–1492.

Mitchell, H. L., Charette, C., Chouinard, C. and Brasnett, B. 1990. Revised interpolation statistics for the Canadian data assimilation procedure: their derivation and application. *Mon. Wea. Rev.* **118**, 1591–1614.

Neiman, P. J. and Shapiro, M. A. 1993. The life cycle of an extratropical marine cyclone. Part I: Frontal-cyclone evolution and thermodynamic air–sea interaction. *Mon. Wea. Rev.* **121**, 2153–2176.

Pedlosky, J. 1979. *Geophysical fluid dynamics.* Springer-Verlag, 624 pp.

Schafer, J. T. and Doswell, C. A. III, 1980. The theory and practical application of antitriptic balance. *Mon. Wea. Rev.* **108**, 746–756.

Shapiro, M. A. and Keyser, D. 1990. Fronts, jet stream and the tropopause. In: *Extratropical cyclones.* The Palmen Memorial Volume. (C. W. Newton and E. Holopainen, Eds.). Amer. Meteor. Soc., Ch. 10, p. 167–179.

Yu, T.-W. and McPherson, R. D. 1984. Global data assimilation experiments with scatterometer winds from SEASAT-A. *Mon. Wea. Rev.* **112**, 368–376.